Lab on a Chip

PAPER

View Article Online
View Journal

Cite this: DOI: 10.1039/c4lc01293c

Fast and cost-effective fabrication of large-area plasmonic transparent biosensor array†

R. Intartaglia,*[a] S. Beke,[a] M. Moretti,[b] F. De Angelis[b] and A. Diaspro[a]

Received 31st October 2014,
Accepted 5th January 2015

DOI: 10.1039/c4lc01293c

www.rsc.org/loc

Surface enhanced Raman-based sensors are widely used for chemical and biological species analysis; but to date the high cost, long production time, hazardous, and toxic content as well as small sensing area and opacity are limiting their capabilities for widespread applications in the medical and environmental fields. We present a novel cost-effective method for fast laser-based fabrication of affordable large-area and transparent periodic arrays of ligand-free metallic nanoparticles, offering a maximum possibility for the adsorption/immobilization of molecules and labeling. Further, we demonstrate a remarkable detection limit in the picomolar range by means of Raman scattering, thus evidencing a superior signal-to-noise ratio compared to other sensor substrates. The high sensitivity performance along with a fast and cheap fabrication procedure of reusable large-area transparent plasmonic devices opens the route for direct, *in situ* multimodal optical analysis with broad applications in the biomedical/analytical fields.

Introduction

Plasmonics is becoming a driving force in the development of various optical devices with broad applications in the fields of biology, chemistry, biosensing, and recently in the development of future solar cells.[1–3] Due to the unique interaction of light with the free surface electrons in the metal nanostructure, known as plasmon resonance, such metallic particles have extremely high scattering and absorption cross-sections. Thus, the local electromagnetic field of incoming light can be remarkably enhanced.[4,5] These phenomena enable metal nanoparticles (NPs) to serve as plasmonic light trapping structures for thin-film solar cell devices, intense labels for immunoassays,[6–8] biochemical sensors,[9–14] and surface-enhanced spectroscopy sensors.[15–22] Among these applications, Surface Enhanced Raman Spectroscopy (SERS) is a highly efficient analytical tool applied in the medical field to study the trace analytes (*e.g.*, urea, citric acid) and chemical changes in blood and urine[23,24] and for the detection of mercury(II) ions in drinking water.[25]

During the past decades, researchers made great efforts to find ideal SERS substrates, mainly including pioneering studies on the preparation of metal nanostructure arrays by various methods,[26–34] such as template-based method,[35] electron beam lithography,[26–28] optical lithography,[29] pulsed laser lithography,[30–34] and hazardous and toxic metallic nano-object deposition on surfaces.[36] These techniques present some limitations or drawbacks, such as high cost, long production time, and critical SERS detection. The SERS detection is mainly limited due to the presence of an artificial ligand in the chemically synthesized nanoparticles and/or chemical linkers to immobilize nanoparticles on the SERS substrate.[37] Another limitation concerns the opacity of these SERS substrates to visible light, which impedes the visualization of the microscopic details of biological substances. In this context, much effort is currently being put in the development of transparent SERS devices, which will open up opportunities for more challenging applications, such as direct, non-invasive and online multimodal optical analyses, *i.e.* simultaneous optical examination of specific biological samples and their SERS characterization in various states. Despite some approaches that are available to make SERS devices transparent, such as low temperature oblique angle deposition[38] and ion drift process,[39] this issue still represents a limitation in this field.

Here we present a comparatively simple approach for the realization of cheap and large-area hydrophobic transparent substrates endowed with good plasmonic functionalities and low detection limits under ligand-free conditions, *i.e.* without stabilizing agents that hinder the detection capabilities. Our fabrication process of transparent plasmonic devices combines different concepts including laser lithography for glass microstructuring,[40–43] laser synthesis of ligand-free nanoparticles in solution phase[44–53] and their assembly by a hydrophobic surface-based strategy.[54,55] Briefly, the mask-projection

[a] *Nanophysics, Istituto Italiano di Tecnologia, via Morego, 30, 16163 Genova, Italy. E-mail: romuald.intartaglia@iit.it*
[b] *Nanostructure, Istituto Italiano di Tecnologia, via Morego, 30, 16163 Genova, Italy*

† Electronic supplementary information (ESI) available. See DOI: 10.1039/c4lc01293c

technique provides prompt (<1 second) surface irradiation inducing photochemical modification in the glass, which is a prerequisite for the fabrication of hydrophobic, transparent, and large-area conical patterns. As to be explained thereafter, the hydrophobic surface enables accurate control of spatial distribution and delivery of ligand-free Au NPs to the surface area (tip of the cones). This approach strongly improves the detection limit with a cleaner signal by reducing the active area of the sensor and chemical effects (bare and clean surface of Au NPs);[37] moreover, it can be extended to large-area processing for mass production. Therefore, the proposed approach can help to overcome all limitations introduced above. The detection efficiency, *i.e.*, the SERS enhancement factor, can be evaluated by using cresyl violet (CV) molecules. The SERS signal is enhanced by three orders of magnitude compared to other SERS-sensitized metallic surfaces. As we report here, the transparent SERS device is able to detect CV molecules at an estimated level of 1 nM within only 100 ms of integration time and very low laser power (55 μW). The collected data suggest that for longer integration time, higher laser power and further optimization, a detection limit far below the picomolar range, can be achieved.

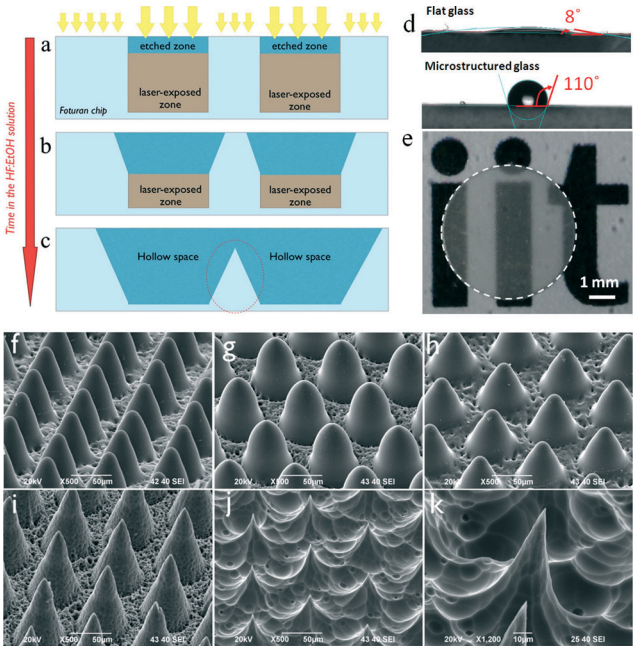

Fig. 1 a–c) Schematic representation of the chemical etching process on the previously laser-exposed and annealed glass chip, *i.e.*, the microtip array formation. Image d) presents the modification of the wettability behavior of the glass surface. The contact angle changes from 8° to 110° due to laser surface microstructuring. Image e) shows an optical microscopy image of the laser-treated glass surface (dashed circle) confirming the preserved transparency of the substrate. The microstructured surface within the dashed circle is presented in figure k). Images (f–k) display various conical structures when using the same mask, but different chemical etching periods, 5, 10, 15, 20, 25, and 30 minutes, respectively. These f–k) images highlight the importance of the etching process which is a crucial experimental step to achieve the desired geometry, height, and aspect ratios.

Results and discussion

Laser fabrication of large-area hydrophobic microtip array

The fabrication of large-area microtip arrays on biocompatible glass is performed in three steps (laser irradiation, annealing, and wet etching). To increase the microtip surface area, only the first step, *i.e.* laser irradiation, has to be scaled up and extended to a larger area by applying a step-and-repeat method for high-throughput production. For instance, an area of 5 × 5 cm^2 would be irradiated in less than 30 seconds. The subsequent annealing and etching steps take about 5 and 0.5 hours, respectively. The time needed for these last two steps doesn't depend on the size of the device. In the first step, excimer laser irradiation of photosensitive glass is applied using a mask projection technique to write latent images/patterns in the glass. The size of the device discussed in the manuscript exhibits a 5 mm-diameter area (see Fig. 1e) and the size can be scaled up to several cm^2 by using multiple laser irradiation in the *XY* plane and/or increasing the laser spot size of the mask-projection system (see Fig. S1a†). Experiments were carried out using a KrF excimer laser operating at 248 nm with a pulse duration of 20 ns and a laser fluence of 0.2 J cm^{-2}, coupled with a micromachining workstation (Micromaster, Optec). A single laser pulse was fired on the glass surface. For mask patterns, lithographic photomasks (chromium on quartz) are used with a pattern corresponding to the desired 3-D geometry to be fabricated in the glass. The resulting latent image in the glass forms a pattern where the center-to-center (center means the final fabricated microtip) distance is determined by the distance "*d*" on the mask divided by 4 due to the 4× demagnification of the mask projection system (Fig. S2†). The second step consists of annealing the glass sample in a programmable furnace to form the crystalline phase of lithium metasilicate. The temperature is first ramped up to 500 °C at 5 °C min^{-1}, held at this temperature for 1 h, then rose to 605 °C at a rate of 3 °C min^{-1}, and held for another hour. In the third step (Fig. 1), the glass chip is immersed in an aqueous solution of 10% hydrofluoric acid (HF) in an ultrasonic bath for selective removal of the laser-exposed zone. During this last process intense etching starts on the laser-exposed region, but at the same time, the unexposed glass surface is also etched. In other words, the etching process promptly starts on the whole glass surface as indicated by the yellow arrows in Fig. 1a. The thinner yellow arrows represent a slower etching rate to which the non laser-exposed glass surface is subjected. The conical array formation, demonstrated in Fig. 1a–c, is a consequence of the different etching periods at different depths inside the glass, *i.e.*, the glass surface on the top is exposed to a longer etching time than the deeper regions, resulting in the formation of conical tips between the laser-exposed zones (Fig. 1c). Microtip arrays with desired geometry and aspect ratios can be realized through the highly time-dependent and accurate etching process. SEM images of

conical arrays with different aspect ratios on the glass surface obtained at different etching times from 10 to 25 minutes are shown in Fig. 1f–j. The appropriate etching conditions are thus crucial for the desired microtip formation. Fig. S2† shows the other embedded structures in the glass, pointing out the versatility and easy realization of the mask-projection technique. As it is well known, the surface roughness allows the control of the wettability properties.

In the present case, the obtained conical surface microstructuring turns the surface wetting properties from hydrophilic to hydrophobic as demonstrated in Fig. 1d. The contact angle measurements show an increase from a value of 8° (on water-flat glass) to 110° (on microstructured glass). Note that hydrophobic surfaces obtained by our method are reproducible and can be scaled up by multiple folds if a step-and-repeat method for high-throughput production is applied. Moreover, as shown in Fig. 1e, the transparency of the laser-treated glass surface with a 5 mm diameter (dashed circle) is preserved.

Self-localization of ligand-free Au nanoparticles on hydrophobic microstructured transparent surface

The realisation of the hydrophobic surface is a key point in the self-localization process of NPs and molecules dissolved in solution. In fact, it enables the self-positioning of the ligand-free NPs or molecules dissolved in aqueous solution.[54,55] Recently, Yang *et al.* reported that analyte molecules could be significantly enriched by using the superhydrophobic surface properties before SERS detection, enabling an extremely sensitive detection of molecules in a highly diluted solution.[56] The deposition method is as follows: a drop of water containing ligand-free Au NPs is deposited onto the microstructured hydrophobic glass, (Fig. 2A). The low adhesion force between the drop, *i.e.*, liquid sample of Au NPs, and the microstructured glass surface allows the drop to evaporate, while shrinking its volume and maintaining its quasi-spherical shape. During the evaporation of the solution of ligand-free Au NPs, the particles become more and more concentrated. At the end of the process, when the shape and concentration reach an unstable condition, the drop collapses and the ligand-free NPs are deposited on the top of the microtips. This procedure can be automated by employing inkjet printers which, when properly optimized, can allow quasi-uniform coverage (by overlapping spotting points) over a large area. For the proof of concept of plasmonic device fabrication, we employed a laser-treated surface displaying hydrophobic properties with 110°, as shown in Fig. 1e. Fig. 2B–D present SEM images of the laser-fabricated hydrophobic microtip array after the self-positioning process of NPs under three magnifications: overview of the 5 mm processed area (Fig. 2B), close-up of the microtip array displaying homogeneous, periodic and conical microstructure (Fig. 2C) and a single microtip with a sub-100 nm-sized tip coated with ligand-free Au NPs (Fig. 2D). As we report below, Raman analysis of several randomly selected microtips

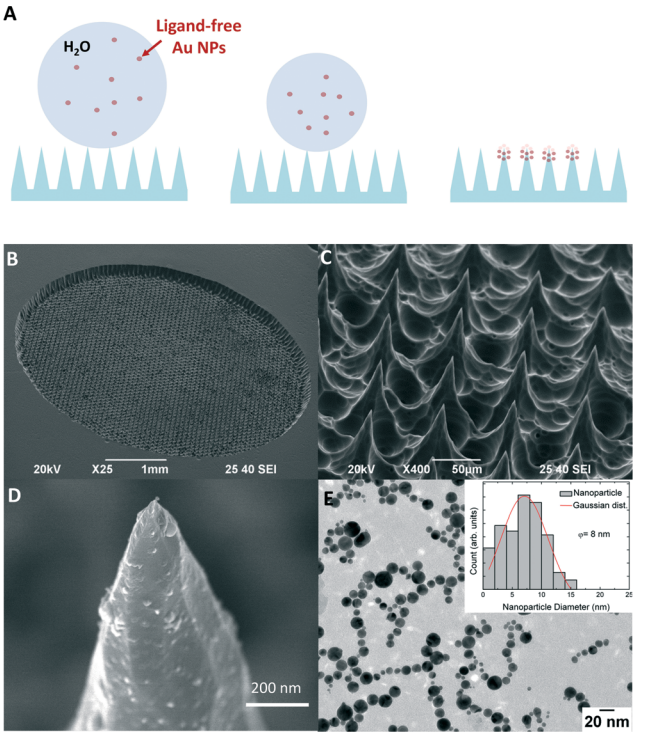

Fig. 2 A) Scheme (not in scale) of drop evaporation on the hydrophobic and transparent surface delivering ligand-free Au NPs to the top of the microtip. SEM images showing the plasmonic microtip sensor array with three magnifications: B) overview of the 5 mm processed area, C) close-up of the microtip array, D) single microtip with a sub-100 nm-sized tip coated with ligand-free Au NPs. E) TEM image of ligand-free Au-NPs prepared by ultrafast pulsed laser ablation in deionized water.

coated with ligand-free Au NPs confirmed the presence and uniformity of nanoparticles over the microstructured area. On the other hand, the sub-100 nm-sized tip together with the ligand-free Au NPs is the key point for good plasmonic functionalities, as discussed in the next section. Ligand-free Au-NPs prepared by femtosecond laser ablation of a gold target in deionized water are reported in Fig. 2D. In the inset, the histogram the NP size distribution is shown, obtained by counting the particles in the electron microscopy image. Isolated 8 nm ligand-free Au NPs with a pseudo-spherical morphology and a smooth surface are obtained, displaying a plasmon resonance peak at around 520 nm (see also the Methods section and Fig. S3†). The feasibility of using a hydrophobic surface-based self-positioning method to assemble the Au NPs on the top of a conical transparent microstructure is supported by optical analysis. One can note that the positioning of ligand-free Au NPs on the top of conical microtips allows the preservation of the transparent properties of plasmonic devices. The total transmission spectra of a flat glass substrate (red line), microstructured glass (blue line), and a conical glass microtip coated with Au-NPs (black line) are presented in Fig. 3. The Au NP-coated microstructured glass-based plasmonic device displays highly transparent properties in the visible spectral

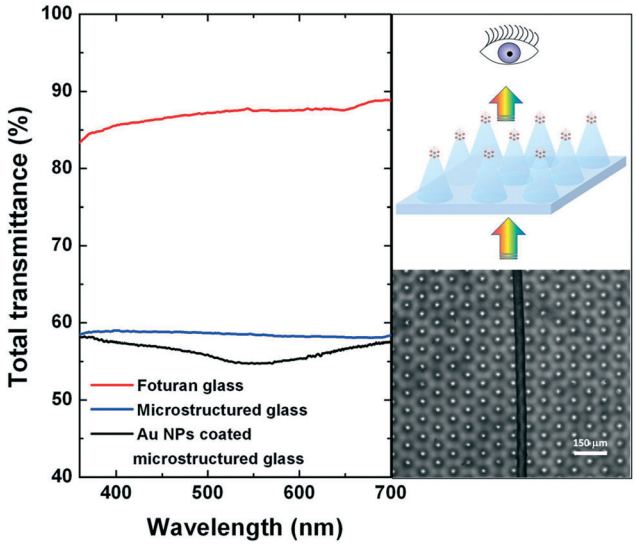

Fig. 3 Total transmittance spectra of a flat glass (red line), a microstructured glass (blue line), and Au NP-coated microstructured glass (black line). On the right side, an optical microscopy image in transmission mode of a human hair deposited on the plasmonic device is shown.

range. Due to the scattering of the microtip arrays, the transmittance of the microstructured glass is lower than that of the original glass. Additionally, the dip observed at 540 nm represents the plasmon resonance of the Au NPs deposited on the top of conical microtips confirming the presence of Au NPs. This characteristic plasmonic feature can be compared with the recently published scattering spectra of similar Au NP arrays deposited randomly on glass substrates.[57] On the right side of Fig. 3, the optical microscopy image in transmission mode of human hair deposited on the plasmonic device is shown. Cellulose fiber deposited on the substrate showcasing the potentiality of the plasmonic device for multimodal optical analysis, *i.e.* visualization and characterization, is presented in Fig. S5.†

Plasmonic features and SERS analyses

The ligand-free Au NPs are anchored by adhesion forces. Once they are delivered they will remain stuck to the surface even when another drop of solution is deposited on the sample. Therefore, the self-positioning process can be repeated again to deliver analytes to the same area where Au NPs are located. This approach strongly improves the detection limit since it reduces the active area of the sensor (thus reducing the background noise) and it allows the delivery of all molecules exclusively to the plasmonic active area, even when highly diluted samples are investigated.[56] We notice that in principle other spectroscopic methods can also be used to detect the liquid sample, such as infrared absorption spectroscopy, fluorescence spectroscopy, mass spectrometry (MALDI) and others. We remark that the protocol is of general validity and in principle also other kinds of NPs can be delivered. However, ligand-free Au NPs represent a successful alternative to the conventional chemically synthesized Au NPs as revealed by detailed Raman studies (Fig. S4†). Ligand-free metallic NPs display a featureless Raman background spectrum (intensity is negligible), while chemically synthesized NPs with an artificial ligand on the NP surface present a strong Raman background signal, thereby limiting the signal-to-noise ratio (Fig. S4†). Consequently, the ligand-free surface of metallic NPs prepared by laser processing increases possibilities for the adsorption/immobilization of molecules and SERS detection by i) the absence of ligands at the surface of NPs which makes the NP surface available to adsorb analytes and ii) reducing the artificial ligand-induced vibration effects, making SERS signals more sensitive and cleaner. The potential of this approach in terms of detection sensitivity was evaluated by using cresyl violet (CV) molecules from water solutions under a concentration of 1 nM. A drop of solution was deposited on three distinct surfaces to compare detection signals: 1) sputtered Au thin film on the flat glass substrate (thickness: 25 nm, reference sample C), 2) sputtered Au thin film on a glass microtip (thickness: 25 nm, sample B), and 3) ligand-free Au NPs anchored on a glass microtip (mean size NP: 8 nm, sample A). As a control, ligand-free Au NPs were deposited on the flat glass substrate. As expected, ligand-free Au NPs were randomly distributed on the glass surface, thus limiting the sensing analysis protocol (data not shown). SERS activity of the transparent plasmonic device was investigated by means of a Renishaw InVia Raman microscope with an objective of 150× (NA – 0.90) at room temperature. The spectra were recorded in backscattering geometry by irradiating it at a wavelength of 633 nm with a maximum power of 55 μW and an acquisition time of 100 ms unless mentioned otherwise. The Raman measurement performed on reference sample C chemisorbed with CV molecules (Fig. 4a) shows a very low intensity Raman band centered at around 592 cm^{-1} even when a very long acquisition time of 50 s was employed. The intensity of this band increased when the SERS measurements were performed on CV deposited on the Au-evaporated microtips (sample B) with 100 ms acquisition time, showing as well the appearance of various characteristic bands of CV molecules. This increase in the SERS signal intensity is associated with an electric field enhancement due to the presence of the microtip structure.[58] In general, the smaller the tip the higher the electric field enhancement is.[59] Further increase in Raman bands' intensity throughout the spectral range was well observed for the microtip device anchored with ligand-free Au-NPs (sample A), again with 100 ms of acquisition time. This increase is associated with microtips affecting the wettability and the evaporation process, thus influencing the co-localization of nanoparticles, *i.e.* a higher electric field induced by the closely packed Au-NPs[60] and analyte molecules. The co-localization of nanoparticles and analyte molecules by using the hydrophobic surface properties before SERS detection enables an extremely sensitive detection of

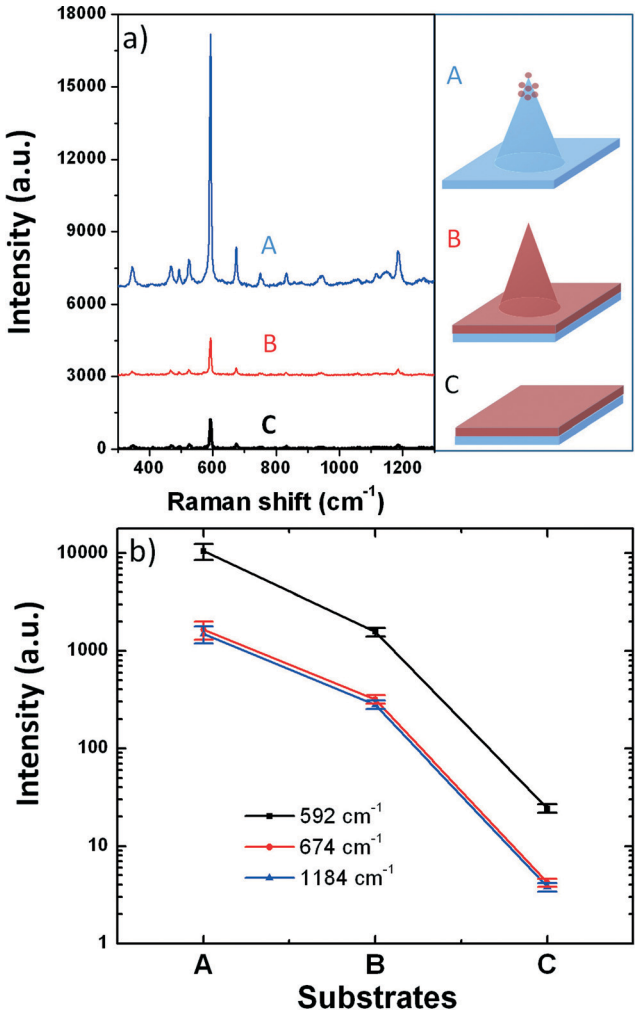

Fig. 4 a) Comparison of Raman spectra with different enhancement substrates: i) ligand-free Au NPs anchored on a microtip (Scheme A, blue line); ii) sputtered rough gold film on the glass microtip (Scheme B, red line); iii) sputtered rough gold film on the glass substrate, reference sample (Scheme C, black line). The detection is evaluated using 1 nM cresyl violet (CV) molecules. The spectra are averaged over several measurements each (λ_{ex} = 633 nm, laser power ~55 μW, integration time: 50 s, 0.1 s and 0.1 s, respectively). b) SERS intensity of the CV characteristic vibrational band when the molecule is deposited over different substrates (laser power: 55 μW, integration time normalized to 0.1 s). For the clarity of the figure, the *Y* axis is in a logarithmic scale. SERS analysis was carried out on three fabricated devices and on several randomly selected microtips over the device area for statistical evaluation. The error bar represents the different values of the obtained SERS intensity.

molecules in a highly diluted solution.[56] These SERS measurements indicate that the amine group of CV (–N–H_2) is attached or is in the vicinity of the Au-NP surface leading to the appearance of the strong Raman scattering. The variation of different bands centered at 592, 674, and 1184 cm^{-1} is shown in Fig. 4b. Raman analysis has been performed on several randomly selected microtips. The resulting SERS signals showed intensities with the same order of magnitude. Additionally, as a control, Raman analysis performed between the microtips confirms the self-localization process of NPs on the top of the microtips (Fig. S6, ESI†). These results confirm thus the presence and the uniform distribution of Au-NPs on the top of microtips over the device area. It is evident from Fig. 4b that even though we don't consider the active area, *i.e.*, number of Au-NPs where the molecules can be adsorbed, the Raman signal enhancement is almost 3 orders of magnitude for sample A compared to that of the reference sample (sample C). The SERS enhancement factor (EF) of Au-NPs anchored to the microtips (sample A) is estimated to be 2.5×10^5 with respect to the Au-coated flat glass substrates, the reference sample (see the ESI† Fig. S6). SERS EF analysis has been performed on several points, *i.e.* different microtips covered with ligand-free Au-NPs. The estimation of the EF value depends on the active surface area, *i.e.* Au-NP density per micrometer squared. One of the most characteristic parameters of a biosensing device is the detection limit. The concerned transparent SERS device is able to detect CV molecules at an estimated level of 1 nM within only 100 ms of integration time and a very low laser power (55 μW). These data suggest that the detection limit can be further improved. For instance, by increasing the integration time to 10 s and the laser power to 0.5 mW (still a reasonable time period in biosensing applications), the detection limit should reach the picomolar range without perturbation from the artificial ligand surrounding the NPs. In principle, by introducing additional possible optimizations (for instance, by altering the conical array density on the substrate), the degree of hydrophobicity could be changed and consequently the detection limit could be improved.[55,56]

Conclusions

We have reported on a simple approach for the realization of cheap and large-area hydrophobic transparent substrates endowed with good plasmonic functionalities and low detection limits under ligand-free conditions. The fabrication process is accomplished by combining i) laser lithography for glass microstructuring, ii) laser synthesis of ligand-free Au nanoparticles in solution phase, and iii) hydrophobic surface-based strategy. Hydrophobic and transparent surfaces with large areas are achieved with homogeneous conical microstructures using our mask projection and etching approaches. The transparent plasmonic device is obtained by dropping a solution of ligand-free Au nanoparticles on the hydrophobic surface which are automatically delivered (self-localization) to the top of the microtips. Our approach emulates other nanoparticle self-localization methods which are costly and more cumbersome to apply and able to deliver analytes only to one single location.[55] In fact, our method strongly improves the detection limit (in the picomolar range) because: 1) it reduces the active area of the sensor, 2) it avoids chemical effects thus reducing the background noise due to bare and clean surface of ligand-free Au NPs, 3) it allows delivery of all analytes to the active plasmonic area (coated with Au NPs) and 4) it can be scaled up by

multiple folds if applying a step-and-repeat method for high-throughput production. We believe that the findings presented here will aid the design of future 3D transparent plasmonic devices as well as disclose the route for several SERS applications for mass production, such as *in situ* and online multimodal optical analysis in the biomedical/analytical field, biology of cell membranes and surfaces, and microfluidics.

Materials and methods

Laser synthesis of ligand-free Au nanoparticles in liquid

The synthesis of ligand-free Au NPs was carried out by femtosecond laser ablation in an aqueous solution (deionized water) as illustrated in the ESI† Fig. S1b. The laser system used in this work consists of a Ti : Sapphire laser with a pulse width of 110 fs centered at 800 nm operating at a repetition rate of 1 kHz. The laser beam is focused using a lens with a focal length of 10 cm onto the Au target (99.999% from Alpha Aesar) placed on the bottom of a quartz cuvette and immersed in 1 ml of liquid medium, deionized water. Before each experiment, the target was mechanically polished and washed several times with the same liquid used for the ablation to remove the impurity from the surface. During the laser ablation, the target was rotated (T-cube DC Servo controller, Thor labs) to achieve uniform irradiation of the gold surface.

NP and plasmonic characterization

The determination of size and size distribution of the Au NPs was performed by transmission electron microscopy (TEM) imaging with a JEOL Jem 1011 microscope working at an acceleration voltage of 100 keV. One drop of the suspension was deposited directly onto a carbon-coated 300 mesh copper grid leaving the solvent to evaporate. Scanning electron microscopy (SEM) using a JEOL JSM-6490 electron microscope was employed for characterization of the samples. The total transmittance spectra were obtained by using a double beam spectrophotometer (Cary 6000i Varian) with an integrating sphere, in the range of 400–700 nm.

References

1 J. N. Anker, W. P. Hall, O. Lyandres, N. C. Shah, J. Zhao and R. P. Van Duyne, *Nat. Mater.*, 2008, **7**, 442–453.
2 H. A. Atwater and A. Polman, *Nat. Mater.*, 2010, **9**, 205–213.
3 D. Qu, F. Liu, J. Yu, W. Xie, Q. Xu, X. Li and Y. Huang, *Appl. Phys. Lett.*, 2011, 98.
4 Y. Xia and N. J. Halas, *MRS Bull.*, 2005, **30**, 338–343.
5 M. C. Daniel and D. Astruc, *Chem. Rev.*, 2004, **104**, 293–346.
6 S. Schultz, D. R. Smith, J. J. Mock and D. A. Schultz, *Proc. Natl. Acad. Sci. U. S. A.*, 2000, **97**, 996–1001.
7 J. M. Nam, C. S. Thaxton and C. A. Mirkin, *Science*, 2003, **301**, 1884–1886.
8 J. Yguerabide and E. E. Yguerabide, *Anal. Biochem.*, 1998, **262**, 137–156.
9 C. R. Yonzon, D. A. Stuart, X. Zhang, A. D. McFarland, C. L. Haynes and R. P. Van Duyne, *Talanta*, 2005, **67**, 438–448.
10 A. J. Haes, L. Chang, W. L. Klein and R. P. Van Duyne, *J. Am. Chem. Soc.*, 2005, **127**, 2264–2271.
11 A. B. Dahlin, J. O. Tegenfeldt and F. Höök, *Anal. Chem.*, 2006, **78**, 4416–4423.
12 A. D. McFarland and R. P. Van Duyne, *Nano Lett.*, 2003, **3**, 1057–1062.
13 R. Elghanian, J. J. Storhoff, R. C. Mucic, R. L. Letsinger and C. A. Mirkin, *Science*, 1997, **277**, 1078–1081.
14 G. Raschke, S. Kowarik, T. Franzl, C. Sönnichsen, T. A. Klar, J. Feldmann, A. Nichtl and K. Kürzinger, *Nano Lett.*, 2003, **3**, 935–938.
15 C. L. Haynes, C. R. Yonzon, X. Zhang and R. P. Van Duyne, *J. Raman Spectrosc.*, 2005, **36**, 471–484.
16 J. A. Dieringer, A. D. McFarland, N. C. Shah, D. A. Stuart, A. V. Whitney, C. R. Yonzon, M. A. Young, X. Zhang and R. P. Van Duyne, *Faraday Discuss.*, 2006, **132**, 9–26.
17 K. L. Haller, L. A. Bumm, R. I. Aitkorn, E. J. Zeman, G. C. Schatz and R. P. Van Duyne, *J. Chem. Phys.*, 1989, **90**, 1237–1252.
18 W. H. Yang, J. Hulteen, G. C. Schatz and R. P. Van Duyne, *J. Chem. Phys.*, 1996, **104**, 4313–4323.
19 T. R. Jensen, R. P. Van Duyne, S. A. Johnson and V. A. Maroni, *Appl. Spectrosc.*, 2000, **54**, 371–377.
20 M. Moskovits, *Rev. Mod. Phys.*, 1985, **57**, 783–826.
21 K. Aslan, J. R. Lakowicz, H. Szmacinski and C. D. Geddes, *J. Fluoresc.*, 2005, **15**, 37–40.
22 Y. Chen, K. Munechika and D. S. Ginger, *Nano Lett.*, 2007, **7**, 690–696.
23 P. D. O'Neal, G. L. Coté, M. Motamedi, J. Chen and W. C. Lin, *J. Biomed. Opt.*, 2003, **8**, 33–39.
24 R. Sulk, C. Chan, J. Guicheteau, C. Gomez, J. B. B. Heyns, R. Corcoran and K. Carron, *J. Raman Spectrosc.*, 1999, **30**, 853–859.
25 L. Wang, T. Li, Y. Du, C. Chen, B. Li, M. Zhou and S. Dong, *Biosens. Bioelectron.*, 2010, **25**, 2622–2626.
26 E. C. Le Ru, P. G. Etchegoin, J. Grand, N. Félidj, J. Aubard, G. Lévi, A. Hohenau and J. R. Krenn, *Curr. Appl. Phys.*, 2008, **8**, 467–470.
27 G. Das, F. Mecarini, F. Gentile, F. De Angelis, H. G. Mohan Kumar, P. Candeloro, C. Liberale, G. Cuda and E. Di Fabrizio, *Biosens. Bioelectron.*, 2009, **24**, 1693–1699.
28 M. G. Banaee and K. B. Crozier, *Opt. Lett.*, 2010, **35**, 760–762.
29 N. M. B. Perney, J. J. Baumberg, M. E. Zoorob, M. D. B. Charlton, S. Mahnkopf and C. M. Netti, *Opt. Express*, 2006, **14**, 847–857.
30 A. Hamdorf, M. Olson, C.-H. Lin, L. Jiang, J. Zhou, H. Xiao and H.-L. Tsai, *Opt. Lett.*, 2011, **36**, 3353–3355.
31 M. J. Beliatis, S. J. Henley and S. R. P. Silva, *Opt. Lett.*, 2011, **36**, 1362–1364.
32 L. Su, T. H. Lee and S. R. Elliott, *Opt. Lett.*, 2009, **34**, 2685–2687.
33 C.-H. Lin, L. Jiang, Y.-H. Chai, H. Xiao, S.-J. Chen and H.-L. Tsai, *Opt. Express*, 2009, **17**, 21581–21589.

34 C.-H. Lin, L. Jiang, J. Zhou, H. Xiao, S.-J. Chen and H.-L. Tsai, *Opt. Lett.*, 2010, **35**, 941–943.
35 S. K. Yang, W. P. Cai, L. C. Kong and Y. Lei, *Adv. Funct. Mater.*, 2010, **20**, 2527–2533.
36 K. C. Grabar, R. G. Freeman, M. B. Hommer and M. J. Natan, *Anal. Chem.*, 1995, **67**, 735–743.
37 R. Intartaglia, G. Das, K. Bagga, A. Gopalakrishnan, A. Genovese, M. Povia, E. Di Fabrizio, R. Cingolani, A. Diaspro and F. Brandi, *Phys. Chem. Chem. Phys.*, 2013, **15**, 3075–3082.
38 J. P. Singh, T. E. Lanier, H. Zhu, W. M. Dennis, R. A. Tripp and Y. Zhao, *J. Phys. Chem. C*, 2012, **116**, 20550–20557.
39 H.-H. Wang, T.-Y. Cheng, P. Sharma, F.-Y. Chiang, S. W.-Y. Chiu, J.-K. Wang and Y.-L. Wang, *Nanotechnology*, 2011, **22**, 385702.
40 S. Beke, L. Korösi, K. Sugioka and K. Midorikawa, *J. Laser Micro/Nanoeng.*, 2012, **7**, 28–32.
41 S. Beke, L. Korösi, K. Sugioka, K. Midorikawa and I. Dékány, *Appl. Phys. A: Mater. Sci. Process.*, 2011, **102**, 265–269.
42 K. Sugioka, M. Masuda, T. Hongo, Y. Cheng, K. Shihoyama and K. Midorikawa, *Appl. Phys. A: Mater. Sci. Process.*, 2004, **79**, 815–817.
43 S. Beke, F. Anjum, L. Ceseracciu, I. Romano, A. Athanassiou, A. Diaspro and F. Brandi, *Laser Phys.*, 2013, **23**, 035602.
44 R. Intartaglia, K. Bagga, F. Brandi, G. Das, A. Genovese, E. Di Fabrizio and A. Diaspro, *J. Phys. Chem. C*, 2011, **115**, 5102–5107.
45 R. Intartaglia, A. Barchanski, K. Bagga, A. Genovese, G. Das, P. Wagener, E. Di Fabrizio, A. Diaspro, F. Brandi and S. Barcikowski, *Nanoscale*, 2012, **4**, 1271–1274.
46 K. Bagga, A. Barchanski, R. Intartaglia, S. Dante, R. Marotta, A. Diaspro, C. L. Sajti and F. Brandi, *Laser Phys. Lett.*, 2013, 10.
47 R. Intartaglia, K. Bagga, A. Genovese, A. Athanassiou, R. Cingolani, A. Diaspro and F. Brandi, *Phys. Chem. Chem. Phys.*, 2012, **14**, 15406–15411.
48 D. M. Popovic, J. S. Chai, A. A. Zekic, M. Trtica, M. Momcilovic and S. Maletic, *Laser Phys. Lett.*, 2013, 10.
49 F. Hajiesmaeilbaigi, A. Mohammadalipour, J. Sabbaghzadeh, S. Hoseinkhani and H. R. Fallah, *Laser Phys. Lett.*, 2006, **3**, 252–256.
50 S. Z. Mortazavi, P. Parvin and A. Reyhani, *Laser Phys. Lett.*, 2012, **9**, 547–552.
51 R. Intartaglia, K. Bagga and F. Brandi, *Opt. Express*, 2014, **22**, 3117–3127.
52 R. Intartaglia, K. Bagga, M. Scotto, A. Diaspro and F. Brandi, *Opt. Mater. Express*, 2012, **2**, 510–518.
53 M. Lau, I. Haxhiaj, P. Wagener, R. Intartaglia, F. Brandi, J. Nakamura and S. Barcikowski, *Chem. Phys. Lett.*, 2014, **610**, 256–260.
54 E. Miele, M. Malerba, M. Dipalo, E. Rondanina, A. Toma and F. De Angelis, *Adv. Mater.*, 2014, **26**, 4179–4183.
55 F. De Angelis, F. Gentile, F. Mecarini, G. Das, M. Moretti, P. Candeloro, M. L. Coluccio, G. Cojoc, A. Accardo, C. Liberale, R. P. Zaccaria, G. Perozziello, L. Tirinato, A. Toma, G. Cuda, R. Cingolani and E. Di Fabrizio, *Nat. Photonics*, 2011, **5**, 683–688.
56 S. K. Yang, P. J. Hricko, P. H. Huang, S. X. Li, Y. H. Zhao, Y. L. Xie, F. Guo, L. Wang and T. J. Huang, *J. Mater. Chem. C*, 2014, **2**, 542–547.
57 D. Gaspar, A. C. Pimentel, T. Mateus, J. P. Leitao, J. Soares, B. P. Falcao, A. Araujo, A. Vicente, S. A. Filonovich, H. Aguas, R. Martins and I. Ferreira, *Sci. Rep.*, 2013, 3.
58 F. De Angelis, C. Liberale, M. L. Coluccio, G. Cojoc and E. Di Fabrizio, *Nanoscale*, 2011, **3**, 2689–2696.
59 R. P. Zaccaria, F. De Angelis, A. Toma, L. Razzari, A. Alabastri, G. Das, C. Liberale and E. Di Fabrizio, *Opt. Lett.*, 2012, **37**, 545–547.
60 F. De Angelis, G. Das, P. Candeloro, M. Patrini, M. Galli, A. Bek, M. Lazzarino, I. Maksymov, C. Liberale, L. C. Andreani and E. Di Fabrizio, *Nat. Nanotechnol.*, 2010, **5**, 67–72.